COMPUTATIONAL ANALYSIS OF COMPRESSIBLE FLUID SPIRAL GROOVE FACE SEALS

Nicole Zirkelback
Dr. Luis San Andrés

April 1997

TRC-SEAL-7-97

COMPUTATIONAL ANALYSIS OF COMPRESSIBLE FLUID SPIRAL GROOVE FACE SEALS

by

Nicole Zirkelback
Graduate Research Assistant
P. I.: Dr. Luis San Andrés

Presented to the 1997 Turbomachinery Research Consortium

EXECUTIVE SUMMARY

Analyses for incompressible and compressible spiral groove thrust bearings (*SGTBs*) and face seals (*SGFSs*) are presented. The non-linear partial differential equation of pressure that arises in the compressible analysis is simplified with a successive approximation. The zeroth- and first-order equations giving the static and dynamic performance of *SGFSs*, respectively, are integrated using the finite element method for both the incompressible and compressible case. A simple thermal coning model proposed in a previous analysis is applied to represent deformation of the seal face due to conduction. Favorable comparisons with the *NGT* and an *FEM* analysis validate the incompressible fluid case for *SGTBs* without inward radial flow. A parametric study indicates effects of changing face seal geometry on the opening force, force coefficients, leakage rate, and power loss and gives the optimum *SGFS* geometry.

TABLE OF CONTENTS

List of Tables

List of Figures

NOMENCLATURE

B	Bearing number; B = -1 ⇒ rotating grooves, B = +1 ⇒ stationary grooves
c	Ridge clearance [m]
c_g	Groove depth [m]
C_{zz}, $\overline{C}_{zz}$	Axial damping coefficient [N·s/m]; $\overline{C}_{zz} = C_{zz} c_g \Omega / W_*$
D_o, D_i, D_{gi}	Outer, inner, groove inner diameter [m]; $D_o = 2 \cdot R_o$; $D_i = 2 \cdot R_i$; $D_{gi} = 2 \cdot R_{gi}$
h	Film thickness [m]; $\overline{h} = h/h_*$
Δh	Outer diameter film thickness change due to thermal deformation [m]
K_{zz}, $\overline{K}_{zz}$	Axial stiffness [N/m]; $\overline{K}_{zz} = K_{zz} c_g / W_*$
$\dot{m}_{r_i}$, $\dot{m}_{\theta_i}$	Dimensionless first-order mass flow rates
N	Speed [rev/s]
N_g	Number of grooves
n_{pe}	Number of nodes per element
P, P_o, $\overline{P}$	Pressures at speed numbers (Λ, Λ_o) [Pa]; $\overline{P} = P/P_*$;
P_*	Incompressible model: $P_* = \mu\Omega\left(R_o/c\right)^2$; compressible model: $P_* = P_a$
ΔP	Pressure variation, $\Delta P = \left.\frac{\partial P}{\partial \Lambda}\right\|_{\Lambda_o} \Delta\Lambda$
P_a, P_{cav}	Ambient, cavitation pressure [Pa]
P_0, P_1	Zeroth and first order pressure fields, [Pa], [Pa/m], [Pa·s/m]
$\wp$	Power loss from friction torque [W]; $\wp = \mathfrak{I}\Omega$; $\overline{\wp} = \wp/\wp_*$; $\wp_* = \pi\mu\Omega^2\left(R_o^4 - R_i^4\right)/2c_g$
Q	Leakage flow rate [ℓ/min]; $\overline{Q} = Q/Q_*$
Q_*	Radial flow for flat circ. plates [ℓ/min]; $Q_* = 6 \times 10^4 \pi c_g^3 \left(P_i - P_o\right)/6\mu \ln\left(r_o/r_i\right)$
q_η	Flow normal to an element
q''	Axial conductive heat flux [W/m^2]
R_i, R_o	Inner and outer seal dam radii, respectively [m]
R_{gi}, R_{go}	Inner and outer groove portion radii, respectively [m]
R_g	Gas constant [J/kg·°C]
(r, Θ, z)	Cylindrical coordinates, groove surface stationary, $\bar{r} = r/R_*$
(r, θ, z)	Cylindrical coordinates, groove surface rotating
$\Re$	Radius ratio; $\Re = R_o/R_i$
S	Sommerfeld number; $S = \mu N \pi R_o^2 \left(R_o/c_g\right)^2 / W$
T	Temperature [°C]
$\mathfrak{I}$	Friction torque [N·m]
t, τ	Time [sec]; $\tau = t\omega$
W, $\overline{W}$	Load [N]; $\overline{W} = W/W_*$; $W_* = \pi\left(R_o^2 - R_i^2\right)\mu\Omega\left(R_o/c_g\right)^2$
W_m^*, $\overline{W}_m$	Dimensionless load defined by Muijderman (1966); $W_m^* = \mu\Omega R_o^4/c^2$; $\overline{W}_m = W/W_m^*$
Z	Complex impedance [N/m]; $Z = K_{zz} + \mathbf{i}\omega C_{zz}$
Δz	Perturbations in axial distance [m]

α_g	Groove width ratio
α_{ex}	Coefficient of thermal expansion [1/°C]
β	Spiral angle [°]; $\beta = 90° \Rightarrow$ radial grooves
Γ^e	Element boundary
δ	Dimensionless groove depth, $\delta = c_g/c + 1$
ε_z	Dimensionless eccentricity; $\varepsilon_z = 1 - c/c_g$
θ	Circumferential coordinate attached to rotating face
Θ	Circumferential coordinate fixed to stationary face, $\Theta = \theta + \Omega t$
κ	Thermal conductivity [W/(m·°C)]
Θ_{g-r}	Arc length of a groove-ridge pair, $\Theta_{g-r} = 2\pi/N_g$
Λ	Speed number $\Lambda = 6\mu\Omega/p_a\left(R/h_*\right)^2$
μ	Fluid viscosity [Pa·s]
ρ	Fluid density [kg/m^3]
ρ_c	Radius of curvature for thermal deformation [m]
σ	Frequency number; $\sigma = 12\mu\omega/p_a\left(R/h_*\right)^2$
$\{\Psi_i\}_{i=1}^{n_{fe}}$	Shape functions within the finite element
ω	Frequency of dynamic motions
Ω	Rotational speed [rad/s]
Ω^e	Finite element sub-domain

Subscripts

gi	Inner radial groove extent
go	Outer radial groove extent
i	Inner radius
o	Outer radius, starting value
0	Zeroth-order
1	First-order
*	Characteristic value

Superscripts

e	Finite element
*	Original value

INTRODUCTION

With the advent of strict mandates from environmental protection laws requiring engineers to virtually eliminate leakage in industrial processes, better sealing technologies must be developed to prevent release of these volatile and potentially dangerous process fluids into the atmosphere. The spiral groove face seal (*SGFS*) offers numerous advantages over conventional contacting mechanical seals. Grooves etched on the mating ring of the sealing surfaces do not wear from contact while rotating, greatly lessening the need to overhaul machines for seal replacement. Dry (gas lubricated) operation allows the face seal to perform with less complicated and expensive external support systems like those required for oil lubricated seals. The use of tandem and double sealing arrangements with inert buffer gases allow application of the *SGFS* in machines handling highly volatile process fluids with virtually zero leakage to the atmosphere.

The first analyses adopted to model thin-film grooved bearing geometries use the Narrow Groove Theory (*NGT*) where an infinite number of grooves is the primary assumption. This analysis as initially applied to parallel, helical groove configurations is mostly found for herringbone grooved journal bearings (*HGJBs*). A detailed review of the pertinent literature for *HGJBs* can be found in Zirkelback and San Andrés (1997). In general, the *NGT* is limited to prediction for concentric journal operation, and although few advances have been made for modeling turbulent flow, the *NGT* is mainly limited to prediction in the laminar flow regime.

The groove shape became the primary concern when applying the *NGT* to spiral groove thrust bearings (*SGTBs*) due to the logarithmic spiral contour of the grooves. Muijderman (1966) presents an extensive *NGT* analysis for various spiral and

herringbone groove thrust bearing configurations including flat, spherical, and conical bearings, and approximate formulae are given for pressure, load capacity, friction torque, and the coefficient of friction for each bearing type. Experiments are also recorded for flat aerostatic *SGTBs*, and comparisons with the given analyses are provided. Although the analyses represent only incompressible fluids, the comparisons prove favorable. Finite differences are applied to solve the Reynolds equation for compressible fluids with constraining jump equations satisfying the discontinuity at the ridge to groove interfaces in *SGTBs* as presented by James and Potter (1967). Attempting to better represent the specfied pressures at the boundaries of *SGFSs*, Sneck and McGovern (1973) introduce the narrow seal theory since the original *NGT* as presented by Muijderman (1966) considers an infinitely wide thrust bearing face without specified boundary pressures. Despite the simplification of straight parallel grooves, the predictions using the narrow seal theory without pressure gradients compare well with results from Muijderman (1966).

As the limitations of the *NGT* became apparent, extensions to the original analysis appeared for various theoretical aspects. Pan and Sternlicht (1967) present a simple heat transfer study that models thermal distortion of flat, ungrooved thrust bearing surfaces, where the drag-induced frictional power dissipation is conducted through the bearing faces. The analysis assumes that heat flow through the faces is uniform and purely axial; however, effects of the groove geometry are neglected in the thermal model since the viscous shear stress is calculated between two flat plates. Considering for both *SGFSs* and Rayleigh step seals, Cheng, et al. (1969) discuss the relative placement of grooves and seal dams within the context of a *NGT* analysis that uses the Reynolds equation for compressible fluids. The authors conclude that seal dams on the low pressure side of the

SGFS minimize leakage at the expense of axial stiffness, while seal dams on the high pressure side give higher values of stiffness. Hsing (1972) extends the *NGT* to include slip flow and turbulence using generalized coordinates to model most groove bearing geometries (*e. g.*, flat, spherical, conical, and cylindrical). Using results obtained previously, Hsing (1974) presents analytical solutions for force coefficients in spiral groove viscous pumps. Furthermore, Sato, et al. (1990) present a simple, incompressible *NGT* analysis in the generalized coordinates provided in Hsing (1972) to obtain the optimum groove geometry for both the *SGTB* and *HGJB* configurations.

Special considerations necessary when dealing with cryogenic liquid oxygen are noted for the design of a particular *SGFS* in Shapiro, et al. (1984). The analysis used applies enhancements to Muijderman's *NGT* in turbulence, fluid inertia, and thermal and elastic deformations to make predictions of film thickness, axial stiffness, leakage, power loss, and temperature rise for increasing rotational speeds. Salant and Homiller (1992) present a finite difference solution of the Reynolds equation for incompressible fluids that accounts for fluid cavitation in upstream pumping *SGFS* operating in both single and double seal configurations. A parametric study reveals instability due to negative stiffness when a *SGFS* operates as a single seal; however, properly designed *SGFSs* remain stable in double seal configurations. Lastly, Kowalski and Basu (1995) optimize the *SGFS* geometry for reverse rotation and forward rotation simultaneously by solving the Reynolds equations for compressible fluids with finite differences. Tests verify the feasibility of meeting the design demands; however, an expected increase in leakage accompanies the optimized bidirectional design (23° groove angle).

Experimental studies in addition to that presented by Muijderman (1966) include tests by James and Potter (1967) performed on a test rig that employs ceramic *SGTBs* and spiral groove compressors with air. The experiments involve measurements of outlet pressure and air flow rate. Static loads with 10% possible error and an optimum geometry are determined from the tests. In a series of reports, DiRusso (1982, 1984, 1985) presents measurements of the film thickness and drag torque for various *SGFS* configurations. The latter two reports (DiRusso, 1984, 1985) concentrate on the dynamic axial oscillations of the seal face and the effects of misalignment while reporting instabilities for outward pumping *SGFS* when the hydrodynamic pressure forces overcome the spring force at seal liftoff. DiRusso (1983) also presents a parametric study using a previous *NGT* study to analytically determine the optimum geometry of *SGFSs*. Experiments presented in Furuishi, et al. (1985) for a *SGTB* operating with water give the load carrying capacity and corresponding minimum film thicknesses for geometries with varying groove depths and support configurations. Different support configurations lessen thermal coning so that experiments match more closely with the simplified *NGT* analysis presented. However, the softer support configurations also diminish the load carrying capacity of the spiral groove thrust bearing.

With its ability to easily represent complicated geometries and any number of grooves, the Finite Element Method (*FEM*) has been the more recent choice for solving the Reynolds equation applied to spiral groove bearing and seal designs. Reddi (1969) and Reddi and Chu (1970) discuss application of the *FEM* to incompressible and compressible fluid spiral groove bearings, respectively. Finite element solutions for load capacity and axial force coefficients are provided by Someya (1989) for an

incompressible fluid *SGTB* having a pressure dam on the bearing inner diameter. Bonneau, et al. (1993) present a finite element model of *SGFSs* that uses upwinding to allow solution of the nonlinear Reynolds equation for compressible fluids. Graphs showing load and leakage rate illustrate the effects of mesh refinement and increased speed numbers.

OBJECTIVE

The present work includes analyses of incompressible as well as compressible fluid *SGFSs* using the finite element method to solve the partial differential equations of hydrodynamic pressure. Analytical perturbations are performed for both cases in order to determine the dynamic axial force coefficients. To allow solution of the non-linear partial differential equation describing compressible fluids in *SGFSs*, the analysis utilizes the successive approximation approach described in Reddy and Chu (1970) to obtain solutions for the zeroth-order (equilibrium) pressure distribution. A simple model of thermal deformation due to conduction through the seal faces is employed since low flow rates out of the seal render convection heat transfer as negligible. Comparisons are made with the *NGT* (Muijderman, 1966) to validate the present incompressible model.

ANALYSIS

Figure 1 shows two configurations of the spiral groove face seal (*SGFS*). In Figure 1.a, the grooved surface is stationary while the flat mating surface rotates (counterclockwise) with speed Ω. The (r, Θ, z) coordinate system, connected to the stationary grooved surface, is used to describe this seal geometry. Figure 1.b shows the

second configuration of the *SGFS* where the grooved surface rotates at speed Ω (clockwise) opposing a stationary, flat mating surface. This configuration is described with a (r, θ, z) coordinate system attached to the rotating, grooved surface.

The coordinate transformation between the two configurations is given by

$$\Theta = \theta + \Omega t \tag{1}$$

and a bearing number (B) of +1 implies stationary grooves while B = -1 denotes rotating grooves. The seal has inner radius R_i denoting the beginning of the inner seal dam and outer radius R_o indicating the end of the outer seal dam. The inner and outer radii for the grooved portion are defined with R_{gi} and R_{go}, respectively. It is assumed that the rotating surface can only move axially so that tilt angles can be neglected. Several descriptive parameters characterize the groove geometry. The ridge clearance (c) plus the groove depth (c_g) give the maximum clearance ($c + c_g$), and the dimensionless groove depth (δ) is described with $\delta = c_g/c + 1$. The width ratio (α_g) is the fraction of the arc length of a groove-ridge pair $\left(\Theta_{g-r} = {}^{2\pi}/_{N_g}\right)$ that is occupied by a groove. The equation governing the logarithmic shape of the grooves is (Muijderman, 1966)

$$r = R_{gi} e^{\theta \tan(\beta)} \tag{2}$$

where the circumferential coordinate is represented by θ and the helix angle (β) is the angle of the groove from the tangent, with $\beta = 90°$ giving radial grooves as illustrated in Figure 2.

Incompressible Fluid Analysis

The lubricating fluid is regarded as incompressible, isoviscous, and newtonian. The appropriate Reynolds equation in cylindrical coordinates describing incompressible, isothermal, laminar, inertialess fluid flow on the seal face is

$$\frac{1}{r}\frac{\partial}{\partial r}\left(\frac{rh^3}{12\mu}\frac{\partial P}{\partial r}\right)+\frac{1}{r}\frac{\partial}{\partial \theta}\left(\frac{h^3}{12\mu r}\frac{\partial P}{\partial \theta}\right)=\frac{\partial h}{\partial t}+B\frac{\Omega}{2}\frac{\partial h}{\partial \theta} \qquad (3)$$

$$0\le\theta\le\Theta_{g-r};\ \ R_i\le r\le R_o$$

Refer to the Nomenclature for proper definitions of all variables. The film thickness h in the equations above is described with

$$h=c \qquad (4.a)$$

in the ridge region and

$$h=c+c_g \qquad (4.b)$$

in the groove region.

The pressure for the seal is specified at the inner and outer radius as, respectively,

$$P\left(R_i,\theta,t\right)=P_i \qquad (5.a)$$

$$P\left(R_o,\theta,t\right)=P_o \qquad (5.b)$$

Since azimuthal thermal distortion and misalignments of the faces are neglected, the circumferential pressure distribution for each groove ridge pair is periodic.

$$P\left(r,\theta_o+n\Theta_{g-r},t\right)_{n=1,\ldots,N_g}=P\left(r,\theta_o,t\right) \qquad (6)$$

Perturbation Analysis

If the rotating surface describes small axial motions (Δz) from an equilibrium position (h_0), the film thickness is equal to

$$h(r,\theta,t) = h_0(r,\theta) + \Delta z\, e^{i\omega t} \tag{7}$$

The effect of these small amplitude motions is to bring perturbations in the pressure about an equilibrium field (P_0), described by the superposition of zeroth- and first-order pressure fields:

$$P(r,\theta,t) = P_0(r,\theta) + P_1 \Delta z\, e^{i\omega t}\ ;\ \mathbf{i} = \sqrt{-1} \tag{8}$$

where P_0 is the zeroth-order pressure field, and P_1 is the perturbed first-order pressure.

With the following definition for the linear differential operator,

$$L(P) = \frac{1}{r}\frac{\partial}{\partial r}\left(\frac{rh^3}{12\mu}\frac{\partial P}{\partial r}\right) + \frac{1}{r}\frac{\partial}{\partial \theta}\left(\frac{h^3}{12\mu r}\frac{1}{\partial \theta}\right) \tag{9}$$

and the substitution of Equations (6) and (7) into the Reynolds Equation (2) gives the zeroth- and first order equations as

Zeroth-Order Equation

$$L(P_0) = B\frac{\Omega}{2}\frac{\partial h_0}{\partial \theta} \tag{10}$$

First-Order Equations

$$L(P_1) = -\frac{1}{r}\frac{\partial}{\partial r}\left(\frac{3rh_0^2}{12\mu}\frac{\partial P_0}{\partial r}\right) - \frac{1}{r^2}\frac{\partial}{\partial \theta}\left(\frac{3h_0^2}{12\mu}\frac{\partial P_0}{\partial \theta}\right) + \mathbf{i}\omega \tag{11}$$

If Δz is arbitrary, it follows that $P_1 = 0$ on the seal boundaries since the inlet and outlet pressures are invariant.

The equilibrium fluid film seal forces (static) acting on the mating surface are obtained from the integration of the zeroth-order pressure field over the area of the seal face:

$$F_0 = N_R \int_{R_i}^{R_o} \int_{0}^{\Theta_{R-r}} P_0 \, r d\theta dr \tag{12}$$

while the stiffness and damping are obtained from real and imaginary parts of first-order pressure field integration,

$$Z = K_{zz} + \mathbf{i}\omega C_{zz} = -N_R \int_{R_i}^{R_o} \int_{0}^{\Theta_{R-r}} P_1 \, r d\theta dr \tag{13}$$

It is important to note that the partial differential equations from which the stiffness and damping coefficients result are not coupled. Hence, the force coefficients are frequency (ω) independent.

To utilize these expressions for forces and force coefficients (Eqns. 12 and 13), the respective pressure fields must be solved. This is accomplished using the finite element method. The program ***spiral.for*** uses the finite element method to solve the zeroth- and first-order pressure equations for a spiral groove face seal with an incompressible fluid using FORTRAN77 in the WINDOWS NT operating system. The finite element method applied to this analysis will now be discussed in more detail.

Finite Element Formulation

The flow domain is discretized into a collection of 4-noded isoparametric finite elements. The pressure over an element is a linear combination of nodal values and shape functions $\{\Psi_i\}$ given by

$$P_0^e = \sum_{i=1}^{n_{pe}} \Psi_i \overline{P}_{0_i}^e \tag{14.a}$$

$$P_1^e = \sum_{i=1}^{n_{pe}} \Psi_i \overline{P}_{1_i}^e \tag{14.b}$$

This allows the differential pressure equations (10, 11) to be reduced into an algebraic system of linear equations. The Galerkin formulation of the zeroth-order pressure equations becomes

$$\sum_{j=1}^{n_{pe}} k_{ij}^e \overline{P}_{0_j}^e = -q_{0_i}^e + f_{0_i}^e \tag{15}$$

where Γ^e is the closure of the element domain Ω^e and

$$k_{ij}^e = \iint_{\Omega^e} \left(\frac{h_0^3}{12\mu} \right)^e \left\{ \frac{\partial \Psi_i}{\partial r} \frac{\partial \Psi_j}{\partial r} + \frac{1}{r^2} \frac{\partial \Psi_i}{\partial \theta} \frac{\partial \Psi_i}{\partial \theta} \right\}^e r d\theta dr \tag{16.a}$$

$$q_{0_i}^e = \oint_{\Gamma^e} \Psi_i^e q_{n_0} d\Gamma^e \tag{16.b}$$

$$f_{0_i}^e = B \frac{\Omega}{2} \iint_{\Omega^e} h_0 \frac{\partial \Psi_i^e}{\partial \theta} r d\theta dr \tag{16.c}$$

Note that once the nodal pressures are known, the flow rates can be obtained from the equation above by solving for $\left\{ q_{0_i}^e \right\}$ along the element boundaries. These equations are condensed by enforcing the corresponding boundary conditions. The result is a symmetric system of equations that are then decomposed and solved to obtain the discrete pressure field.

The first-order equations are obtained and solved in a similar manner. For finding P_1, the corresponding first-order element equations become:

$$\sum_{j=1}^{n_{pe}} k_{ij}^{e} \overline{P}_{1_j}^{e} = -q_{1_i}^{e} + f_{1_i}^{e} - \sum_{j=1}^{n_{pe}} S_{ij}^{e} \overline{P}_{0_j}^{e} \tag{17}$$

where

$$q_{1_i}^{e} = \oint_{\Gamma^e} \Psi_i^e q_{n_2} d\Gamma^e \tag{18.a}$$

$$f_{1_i}^{e} = \iint_{\Omega^e} \left[B \frac{\Omega}{2} \frac{\partial \Psi_i^e}{\partial \theta} - \mathbf{i}\omega \partial \Psi_i^e \right] r d\theta dr \; ; \qquad \mathbf{i} = \sqrt{-1} \tag{18.b}$$

$$S_{ij}^{e} = \iint_{\Omega^e} \left(\frac{3h_0^2}{12\mu} \right)^e \left\{ \frac{\partial \Psi_i}{\partial r} \frac{\partial \Psi_j}{\partial r} + \frac{1}{r^2} \frac{\partial \Psi_i}{\partial \theta} \frac{\partial \Psi_i}{\partial \theta} \right\}^e r d\theta dr \tag{18.c}$$

Compressible Fluid Analysis

If the fluid within the seal is considered as an (compressible) ideal gas at constant temperature, the density is directly proportional to the pressure of the fluid, or

$$\rho = \frac{P}{R_g T} \tag{19}$$

where the quantity $R_g T$ is constant if the temperature (T) does not change. The Reynolds equation in cylindrical coordinates for an isoviscous and newtonian fluid sustaining isothermal, laminar, inertialess fluid flow on the seal face is

$$\frac{1}{r}\frac{\partial}{\partial r}\left(\frac{P r h^3}{12\mu} \frac{\partial P}{\partial r} \right) + \frac{1}{r}\frac{\partial}{\partial \theta}\left(\frac{P h^3}{12\mu r} \frac{1}{r} \frac{\partial P}{\partial \theta} \right) = \frac{\partial P h}{\partial t} + B \frac{\Omega}{2} \frac{\partial P h}{\partial \theta} \tag{20}$$
$$0 \le \theta \le \Theta_{g-r}; \quad R_i \le r \le R_o$$

The same film thickness expressions and boundary conditions as in the incompressible case apply. (See Eqns. 4 through 6.) The method for solution of this non-linear partial differential equation is detailed in Reddy and Chu (1970) where a successive

approximation scheme is proposed. Equation (20) can be rewritten in dimensionless form as

$$\bar{\nabla}\cdot\left(\bar{h}^3\bar{P}\bar{\nabla}\bar{P}\right)=\frac{B}{\bar{r}}\frac{\partial}{\partial\theta}\left(\Lambda\bar{r}\bar{h}\bar{P}\right)+\sigma\frac{\partial}{\partial\tau}\left(\bar{P}\bar{h}\right) \tag{21}$$

where the speed number (Λ) and the frequency number (σ) are described with

$$\Lambda=\frac{6\mu\Omega}{P_*}\left(\frac{R_*^2}{h_*^2}\right) \tag{22.a}$$

$$\sigma=2\Lambda\left(\frac{\omega}{\Omega}\right)=\frac{12\mu\omega}{P_*}\left(\frac{R_*^2}{h_*^2}\right) \tag{22.b}$$

and the subscript (*) denotes characteristic values. (Bars indicating dimensionless values are dropped in subsequent parts of the compressible analysis for simplicity.) Considering a perturbation in space of the speed number, *i. e.*,

$$\Lambda=\Lambda_o+\Delta\Lambda \tag{23}$$

the linearization of pressure (as a function of speed) about this point gives

$$P(\Lambda)=P\left(\Lambda_o\right)+\left.\frac{\partial P}{\partial\Lambda}\right|_{\Lambda_o}\Delta\Lambda \tag{24.a}$$

or

$$P=P_o+\Delta P \tag{24.b}$$

where P_o satisfies the steady-state form of Eqn. (21) for speed number Λ_o. Neglecting derivatives of time for steady-state operation, substitution of the perturbed speed and pressure (Eqns. 23 and 24) into the dimensionless Reynolds Equation (21) gives

$$\bar{\nabla}\cdot\left(h^3\bar{\nabla}PP_o\right)=\frac{B}{r}\frac{\partial}{\partial\theta}rh\left(\Lambda_oP+P_o\Lambda\right) \tag{25}$$

which is now a linear partial differential equation. For two sufficiently close values of (Λ, Λ_o), the successive approximation determines a sequence of pressures until the steady state form is satisfied, *i. e.*,

$$\bar{\nabla}\cdot\left(h^3\bar{\nabla}P^2\right)=\frac{B}{r}\frac{\partial}{\partial\theta}\left[rh(2\Lambda P)\right] \tag{26}$$

Once this equilibrium pressure is determined, the forces and force coefficients can then be obtained.

Perturbation Analysis (Dimensionless Variables)

If the rotating surface describes small axial motions (Δz) from an equilibrium position (h_0) at a frequency (ω), the film thickness is equal to

$$h(r,\theta,\tau)=h_0(r,\theta)+\Delta z\, e^{i\tau} \quad ; \quad \mathbf{i}=\sqrt{-1} \tag{27}$$

where $\tau=\omega\cdot t$ is the dimensionless time. The effect of these small amplitude motions is to bring perturbations in the pressure about an equilibrium field (P_0), described by the superposition of zeroth- and first-order pressure fields:

$$P(r,\theta,t)=P_0(r,\theta)+P_1(r,\theta)\Delta z\, e^{i\tau} \tag{28}$$

where P_0 is the zeroth-order pressure field, and P_1 is the perturbed first-order pressure.

With substitution of the perturbed film thickness (Eq. 27) and pressure (Eq. 28) into the dimensionless Reynolds equation (Eq. 21), the first-order non-linear partial differential equation of pressure becomes

$$\begin{aligned}&\frac{1}{r}\frac{\partial}{\partial r}\left(r\dot{m}_{r_1}\right)+\frac{1}{r}\frac{\partial}{\partial\theta}\left(\dot{m}_{\theta_1}\right)+\mathbf{i}\sigma\left(P_1h_0+P_0\right)=0\\&0\le\theta\le\Theta_{g-r};\quad R_i/r_*\le r\le R_o/r_*\end{aligned} \tag{29}$$

where the first-order mass flow rates are

$$\dot{m}_{r_1} = -\left(3h_0^2 P_0 \frac{\partial P_0}{\partial r} + h_0^3 P_1 \frac{\partial P_0}{\partial r} + h_0^3 P_0 \frac{\partial P_1}{\partial r} \right) \tag{30.a}$$

$$\dot{m}_{\theta_1} = -\left(3h_0^2 P_0 \frac{\partial P_0}{r\partial \theta} + h_0^3 P_1 \frac{\partial P_0}{r\partial \theta} + h_0^3 P_0 \frac{\partial P_1}{r\partial \theta} \right) + B\Lambda r\left(P_0 + h_0 P_1 \right) \tag{30.b}$$

Integration of the first-order pressure field gives stiffness (real part) and damping (imaginary part) coefficients, together representing a complex impedance

$$Z = \overline{K}_{zz} + \mathbf{i}\sigma\overline{C}_{zz} = -N_g \int_{R_i/r_o}^{R_o/r_o} \int_{0}^{\Theta_{g-r}} P_1 \, r d\theta dr \tag{31}$$

Note that once the first-order pressure field is solved and integrated, the stiffness and damping coefficients will be coupled and dependent on the excitation frequency (σ).

Like in the incompressible fluid analysis, the zeroth- and first-order pressures are integrated to obtain the load capacity and dynamic force coefficients, respectively, of compressible fluid *SGFSs*. The finite element method is again applied to solve the non-linear partial differential equations of pressure in the program ***spiralc.f90*** (currently under development) written in FORTRAN90 within the WINDOWS NT operating system.

Finite Element Formulation

The finite element analysis develops for the compressible case in the same manner as before. However, it should be noted that the flow equations are non-linear though effectively linearized by the successive approximation method. The Galerkin formulation of the zeroth-order pressure equations becomes

$$\sum_{j=1}^{n_{pe}} k_{0_{ij}}^{e} \overline{P}_{0_j}^{e} = -q_{0_i}^{e} + f_{0_i}^{e} \tag{32}$$

where Γ^e is the closure of the element domain Ω^e and

$$k_{0_{ij}}^{e} = \iint_{\Omega^e} \left\{ h_0^3 \left[\left(\frac{\partial \Psi_i}{\partial r} \frac{\partial \Psi_j}{\partial r} + \frac{1}{r^2} \frac{\partial \Psi_i}{\partial \theta} \frac{\partial \Psi_j}{\partial \theta} \right) P_\sigma + \left(\frac{\partial \Psi_i}{\partial r} \frac{\partial P_\sigma}{\partial r} + \frac{1}{r^2} \frac{\partial \Psi_i}{\partial \theta} \frac{\partial P_\sigma}{\partial \theta} \right) \Psi_j \right] - Bh\Lambda \frac{\partial \Psi_i}{\partial \theta} \Psi_j \right\} r d\theta dr \tag{33.a}$$

$$q_{0_i}^{e} = \oint_{\Gamma^e} \Psi_i^e \dot{m}_{0_n} d\Gamma^e \tag{33.b}$$

$$f_{0_i}^{e} = \iint_{\Omega^e} Bh_0 \Lambda_\sigma P_\sigma \frac{\partial \Psi_i^e}{\partial \theta} r d\theta dr \tag{33.c}$$

where

$$P_\sigma = \sum_{k=1}^{n_{pe}} \Psi_k P_{\sigma_k} \tag{33.d}$$

The result of these equations due to fluid compressibility renders an asymmetric system of algebraic equations that are then decomposed and solved to obtain the discrete pressure field.

The first-order equations are obtained and solved in a similar manner. For finding P_1, the corresponding first-order element equations become:

$$\sum_{j=1}^{n_{pe}} k_{1_{ij}}^{e} \overline{P}_{1_j}^{e} = -q_{1_i}^{e} + f_{1_i}^{e} \tag{34}$$

where

$$k_{ij}^{e}=\iint_{\Omega^e}\left\{h_0^3\left[\left(\frac{\partial\Psi_i}{\partial r}\frac{\partial\Psi_j}{\partial r}+\frac{1}{r^2}\frac{\partial\Psi_i}{\partial\theta}\frac{\partial\Psi_i}{\partial\theta}\right)P_0+\left(\frac{\partial\Psi_i}{\partial r}\frac{\partial P_0}{\partial r}+\frac{1}{r^2}\frac{\partial\Psi_i}{\partial\theta}\frac{\partial P_0}{\partial\theta}\right)\Psi_j\right]\right.$$
$$\left.-\left[\left(B\Lambda\frac{\partial\Psi_i}{\partial\theta}-\mathbf{i}\sigma\Psi_i\right)h_0\Psi_j\right]\right\}\,rd\theta dr \qquad \textbf{(35.a)}$$

$$q_{ij}^{e}=\oint_{\Gamma^e}\Psi_i^e\bar{m}_1\cdot\bar{\eta}\;d\Gamma^e \qquad \textbf{(35.b)}$$

$$f_{ij}^{e}=-\iint_{\Omega^e}\left\{3h_0^2P_0\left[\frac{\partial\Psi_j}{\partial r}\frac{\partial P_0}{\partial r}+\frac{1}{r^2}\frac{\partial\Psi_i}{\partial\theta}\frac{\partial P_0}{\partial\theta}\right]\right.$$
$$\left.+P_0\left[B\Lambda\frac{\partial\Psi_i}{\partial\theta}+\mathbf{i}\sigma\Psi_i\right]\right\}rd\theta dr \qquad \textbf{(35.c)}$$

where

$$P_0=\sum_{k=1}^{n_{pe}}P_0\Psi_k \qquad \textbf{(35.d)}$$

Note that P_0 in these equations is the zeroth-order discrete pressure field previously solved with the successive approximation approach at speed number Λ. Like in the zeroth-order finite element equations, the resulting algebraic system of first-order equations is also asymmetric.

A Simple Model for Thermal Coning

Thermal coning is accounted for in the present analysis for *SGFSs* by following the procedure given in Pan and Sternlicht (1967) where the radius of curvature due to purely axial heat flux (q'') due to conduction is

$$\frac{1}{\rho_c}=\frac{\alpha_{ex-1}}{\kappa_1}q_1''+\frac{\alpha_{ex-2}}{\kappa_2}q_2'' \qquad \textbf{(36)}$$

where the subscripts 1 and 2 denote differing seal and mating surface materials each with thermal expansion coefficient (α_{ex}) and thermal conductivity (κ). Equation (38) assumes that the thrust bearing or face seal plate is a hollow disk and radial lines deform into circular arcs with radii (ρ_c).

Since the amount of convective heat transfer is insignificant in a gas bearing, all heat transfer is assumed to occur due to conduction through the seal surfaces. The total heat flux through the seal surface is

$$q'' = \frac{\wp}{\pi\left(R_o^2 - R_i^2\right)} \tag{37}$$

where $\wp = \mathfrak{T}\cdot\Omega$ is the power loss due to friction torque ($\mathfrak{T}$). Defining the radius ratio $\Re$ as (R_o/R_i) and applying the following definition,

$$\Delta h = \frac{R_o^2}{2\rho_c} \tag{38}$$

substitution of Eq. (37) into Eq. (38) gives the change in film thickness at the outer radius (Δh) due to curvature of the seal face as

$$\Delta h = \left(\frac{\alpha_{ex\text{-}1}}{\kappa_1} + \frac{\alpha_{ex\text{-}2}}{\kappa_2}\right)\left[\frac{\wp}{2\pi\left(1-\Re^2\right)}\right] \tag{39}$$

Results and Discussion

Comparison with Muijderman (1966)

Muijderman (1966) provides analytical solutions for *SGTBs* that operate with incompressible, isoviscous lubricants using the *NGT*, where the pressure variation between grooves and ridges is simplified into an average, smoothed pressure.

Additionally, the supposition that there is no radial (inward) flow arises since the thrust bearing configurations as studied by Muijderman (1966) have the inward pumping spiral groove thrust plate underneath a flat rotating thrust collar, thus contributing a pressure buildup at the inner diameter (rather than a specified inner diameter pressure) and an additional reaction load (due to the plenum pressure) generated within the inner diameter of the thrust plate. Problems result since the present analysis usually requires specified pressures at the inner and outer diameters *a priori*, and for present applications of *SGFSs* in tandem and double seal configurations, specified boundary pressures at the inner and outer diameters depict a more realistic fluid flow representation. However, a modified version of ***spiral.for*** (incompressible fluid) restricts the flow rate at the inner diameter to zero to enable comparison. (A sample calculation of the pressure and load calculations according to Muijderman (1966) can be found in the Appendix.) The results of the comparisons between the *NGT* and present *FEM* computations* for dimensionless optimum load capacity as the radius ratio ($1/\Re = R_i/R_o$) increases is shown in Figure 3. The characteristic load is defined in this figure as

$$W_m^* = \frac{\mu\Omega R_o^4}{c^2} \tag{40}$$

so that the dimensionless load $\left(\overline{W_m}\right)$ represents the quotient of the calculated load (W) and the characteristic load (W_m^*). Each point in the figure represents the conditions for maximum load capacity as given in Muijderman (1966), and the dimensionless parameters are provided for each case. Note that the total load capacity is the sum of the hydrodynamic load generated by the grooves and the hydrostatic load from the pressure

* FEM parameters used for computations: Radial elements = 50; Circ. Elements (groove, ridge) = 10, 10.

buildup within the inner diameter ($\pi R_i^2 P_i$). Although comparisons are very close, the *NGT* tends to slightly overpredict the load capacity of the *SGTB*, a fact well reported in the literature.

As well as providing analytical calculations for load capacity, Muijderman (1966) gives an estimation of the mean inner diameter pressure using the *NGT*. The actual pressure variations between grooves and ridges as calculated by the *FEM* program is given in Figure 4 with *NGT* pressure calculations included. As expected, the variation in pressure is large for smaller numbers of grooves. As the number of grooves nears infinity (~50), the pressure variation is practically negligible.

Dimensionless dynamic force coefficients are given in Figure 5 for the same geometries. Since in SGTB load is generated over the entire bearing area, the characteristic load used in making the force coefficients dimensionless is

$$W_* = \pi R_o^2 \mu \Omega \left(R_o / c_g \right)^2 \tag{41}$$

As shown, the stiffness $\left(\overline{K}_{zz}\right)$ remains virtually constant while the damping $\left(\overline{C}_{zz}\right)$ coefficients decrease as the radius ratio increases, indicating that using narrower thrust bearing plates may be an undesirable practice. A smaller number of grooves is preferred since the thrust bearing exhibits more stiffness and damping as the number of grooves decreases.

Comparison with Someya (1989)

Figure 6 presents comparison of the present *FEM* analysis against *FEM* calculations of dimensionless eccentricity (ε_z) as the Sommerfeld number (S) increases

given in Someya (1989) for *SGTBs* with pressure dams inside the inner diameter. As defined, the Sommerfeld number (S) represents the inverse of load (W) while the inverse of the ridge (minimum) clearance (c) is designated by the eccentricity (ε_z). The trends[†] show that as the load increases (decreasing S) the ridge clearance decreases (increasing ε_z). Comparisons give very little discrepancy with an average difference of 5.75%.

Parametric Study of a Spiral Groove Face Seal

Variation of the dimensionless force coefficients, leakage rate, and power loss with changes in the *SGFS* geometry is given in Figures 7 through 11. Table 1 shows how the geometry varies in each case. Although the analysis used to compute the results is for incompressible fluids only, nitrogen gas was used in these cases at low speed numbers ($\Lambda < 6$), where this gas acts as an incompressible fluid. These cases are distinct from those presented by Muijderman (1966) since there exists a pressure differential from the outer to inner diameter, *i. e.*, $P_o > P_i$. It should be noted in the figures that the dimensionless leakage rate $\left(\overline{Q} = Q/Q_*\right)^{\ddagger}$ is multiplied by 100 so its order is about unity, which indicates the leakage in *SGFSs* is 100 times less that the leakage of two flat plates with the same order of clearance. The results present the obvious advantage of grooved geometries over conventional non-grooved configurations.

As the number of grooves (N_g) increases in Figure 7, the stiffness and damping coefficients $\left(\overline{K}_{zz}, \overline{C}_{zz}\right)$ and the power loss $\left(\overline{\wp}\right)$ increase slightly while the leakage rate $\left(\overline{Q}\right)$ drops considerably. The behavior of the leakage indicates the effectiveness of

[†] FEM parameters: Radial elements (groove, dam) = 40, 5; Circ. Elements (groove, ridge) = 10, 10

inward pumping grooves since more grooves contain more fluid outward. The opening force (not shown) does not change $\left(\overline{W} \cong 1.19\right)$ with an increase in the number of grooves (N_g).

Figure 8 shows that the stiffness coefficient $\left(\overline{K}_{zz}\right)$ reaches a maximum at a groove angle (β) of 20° while the damping coefficient $\left(\overline{C}_{zz}\right)$ and power loss $\left(\overline{\wp}\right)$ decrease as the groove angle (β) increases. The leakage rate $\left(\overline{Q}\right)$ increases slightly as the groove angle (β) increases. When the groove angle approaches radial grooves $(\beta \rightarrow 90°)$, less seal area exists over which the pressure can develop, and the grooves do not pump fluid inward as well explaining the drop in stiffness and increase in leakage at higher groove angles (β). On the other hand, grooves that are nearly tangential $(\beta \rightarrow 0°)$ do not develop pressure efficiently.

A relatively small seal dam (with ridge clearance, c) inside the inner groove diameter significantly influences the behavior of *SGFSs* as shown in Figure 9. The opening force $\left(\overline{W}\right)$, direct stiffness coefficient $\left(\overline{K}_{zz}\right)$, and damping coefficient $\left(\overline{C}_{zz}\right)$ increase significantly with the introduction of a seal dam. The direct stiffness coefficient also reaches a maximum value at a grooved diameter ratio (D_{gi}/D_o) of 0.55 and falls as the seal dam extends over more of the seal face. The leakage rate $\left(\overline{Q}\right)$ drops considerably until a grooved diameter ratio (D_{gi}/D_o) of 0.65 where the slope of the flow rate appears to become more level, while the power loss $\left(\overline{\wp}\right)$ significantly lowers only until a grooved diameter ratio (D_{gi}/D_o) of 0.55. Since the seal dam has the same clearance

---

‡ Q_* is the flow rate for two flat plates having the same dimensions as the SGFS with clearance c_g.

as the ridge (minimum) film clearance (c), a more extensive seal dam represents a reduction in the average film clearance over the entire seal. Thus, the stiffness coefficient $\left(\overline{K}_{zz}\right)$ and opening force are expected to increase as the grooved extent increases, and the leakage $\left(\overline{Q}\right)$ should decrease. With less grooved area to pump fluid outward, the stiffness coefficient $\left(\overline{K}_{zz}\right)$ decreases when the seal dam becomes too large compared to the grooved part of the seal.

Changes in the groove width ratio (α_g), given in Figure 10, do not significantly change the parameters of interest, although the leakage rate $\left(\overline{Q}\right)$ does increase slightly as the groove width ratio (α_g) increases. Again, this effect can be illustrated by the general increase in the seal average clearance which may increase the amount of leakage $\left(\overline{Q}\right)$ out of the seal.

Figure 11 shows the effect of increasing the groove depth ratio (c_g/c). Since the definitions of the dependent dimensionless parameters depend on the groove depth (c_g), the parameters were made dimensionless using the ridge clearance (c), which is held constant, rather than the groove depth (c_g), as in all other cases. Thus, trends of the dependent dimensionless parameters are preserved. The stiffness $\left(\overline{K}_{zz}\right)$ and damping $\left(\overline{C}_{zz}\right)$ coefficient decrease with the groove depth ratio while the leakage rate $\left(\overline{Q}\right)$ increases. The dependence of the parameters on the groove depth can be generally inferred by realizing that an increase in the groove depth ratio (c_g/c) represents an increase in the average seal clearance. The power loss $\left(\overline{\wp}\right)$ remains constant with the groove depth ratio.

Conclusions

The present work analyses the incompressible and compressible fluid flows in spiral groove thrust bearings and face seals using the Reynolds equation for laminar flow. Since the Reynolds equation becomes a non-linear partial differential equation of pressure in the compressible fluid analysis, a successive approximation allows an iterative solution of an intermediate linear partial differential equation. Discretization of the zeroth- and first-order pressure fields and integration of the partial differential equations of pressure is achieved using the finite element method. A simple thermal coning model calculates deformation of the seal face due to axial conduction; however, examples are not included in the present work. Comparisons of the present analysis (for *SGTBs*) with the *NGT* prove for load capacity and inner diameter pressure favorable, and as expected, the inner diameter pressure variations become significant as the number of grooves lessens. In general, damping force coefficients decrease as the ratio between seal inner and outer radii increases. Finite element calculations given in Someya (1989) for Sommerfeld number further validate the present work. A parametric study shows the effect of varying the *SGFS* geometry on the opening force, force coefficients, leakage rate, and power loss. For a face seal having an inner diameter that is half of the outer diameter, the optimum geometry determined from this study is: $N_g = 12$; $\beta = 20°$; $D_{gi}/D_o = 0.6$, $\alpha = 0.45$; and $\delta \equiv 3$.

REFERENCES

Bonneau, D., J. Huitric, and B. Tournerie, 1993, "Finite Element Analysis of Grooved Gas Thrust Bearings and Grooved Gas Face Seals," *ASME Journal of Tribology*, Vol. 115, pp. 348 - 354.

Cheng, H. S., V. Castelli, and C. Y. Chow, 1969, "Performance Characteristics of Spiral-Groove and Shrouded Rayleigh Step Profiles for High-Speed Noncontacting Gas Seals," *ASME Journal of Lubrication Technology*, Vol. 91, pp. 60 - 68.

DiRusso, E., 1982, "Film Thickness Measurement for Spiral Groove and Rayleigh Step Lift Pad Self-Acting Face Seals," *NASA Technical Paper* 2058.

DiRusso, E., 1983, "Design Analysis of a Self-Acting Spiral-Groove Ring Seal for Counter-Rotating Shafts," *NASA Technical Paper* 2142.

DiRusso, E., 1984, "Dynamic Behavior of Spiral-Groove and Rayleigh-Step Self-Acting Face Seals," *NASA Technical Paper* 2266.

DiRusso, E., 1985, "Dynamic Response of Film Thickness in Spiral-Groove Face Seals," *NASA Technical Paper* 2544.

Furuishi, Y., T. Suganami, S. Yamamoto, and K. Tokumitsu, 1985, "Performance of Water-Lubricated Flat Spiral Groove Bearings," *ASME Journal of Tribology*, Vol. 107, pp. 268 - 272.

Hsing, F. C., 1972, "Formulation of a Generalized Narrow Groove Theory for Spiral Grooved Viscous Pumps," *ASME Journal of Lubrication Technology*, Vol. 94, pp. 81 - 85.

Hsing, F. C., 1974, "Analytical Solutions for Incompressible Spiral Groove Viscous Pumps," *ASME Journal of Lubrication Technology*, pp. 1 - 5. (?)

James, D. D., and A. F. Potter, 1967, "Numerical Analysis of the Gas-Lubricated Spiral-Groove Thrust Bearing-Compressor," *ASME Journal of Lubrication Technology*, Vol. 89, pp. 439 - 444.

Kowalski, C. A., and P. Basu, 1995, "Reverse Rotation Capability of Spiral-Groove Gas Face Seals," *Tribology Transactions*, Vol. 38, No. 3, pp. 549 - 556.

Muijderman, E. A., 1966. *Spiral Groove Bearings*. Philips Technical Laboratory. New York: Springer-Verlag Inc.

Pan, C. H. T., and B. Sternlicht, 1967, "Thermal Distortion of Spiral-Grooved Gas-Lubricated Thrust Bearing Due to Self-Heating," *ASME Journal of Lubrication Technology*, Vol. 89, pp. 197 - 202.

Reddi, M. M., 1969, "Finite Element Solution of the Incompressible Lubrication Problem," *ASME Journal of Lubrication Technology*, Vol. 91, pp. 529 - 533.

Reddi, M. M., and T. Y. Chu, 1970, "Finite Element Solution of the Steady-State Compressible Lubrication Problem," ASME Journal of Lubrication Technology, Vol. 92, pp. 495 - 503.

Reddy, J. N. *Introduction to the Finite Element Method. Second Edition.* New York: McGraw-Hill, 1993; pp. 246 - 249.

Salant, R. F., and S. J. Homiller, 1992, "The Effects of Shallow Groove Patterns on Mechanical Seal Leakage," *Tribology Transactions*, Vol. 35, No. 1, pp. 142 - 148.

Sato, Y., K. Ono, and A. Iwama, 1990, "The Optimum Groove Geometry for Spiral Groove Viscous Pumps," *ASME Journal of Tribology*, Vol. 112, pp. 409 - 414.

Shapiro, W., J. Walowit, and H. F. Jones, 1984, "Analysis of Spiral-Groove Face Seals for Liquid Oxygen," *ASLE Transactions*, Vol. 27, No. 3, pp. 177 - 188.

Sneck, H. J., and J. F. McGovern, 1973, "Analytical Investigation of the Spiral Groove Face Seal," *ASME Journal of Lubrication Technology*, Vol. 95, pp. 499 - 509.

Someya, T. (editor), 1989, *Journal-Bearing Databook*. Berlin: Springer-Verlag. pp. 188 - 190.

Zirkelback, N., and L. San Andrés, 1997, "Finite Element Analysis of a Herringbone Groove Journal Bearing: A Parametric Study," Accepted for publication in the *ASME Journal of Tribology*, April.

Table 1. Parametric study variations for SGFSs operating with incompressible nitrogen gas.

Variation	N_g	β [°]	D_{gi}/D_o	α_g	δ
Figure 7. Number of grooves	6 → 18	20	.74	.5	3
Figure 8. Groove angle	12	10 → 30	.74	.5	3
Figure 9. Grooved diameter ratio	12	20	.5 → .82	.5	3
Figure 10. Groove width ratio	12	20	.74	.45 → .65	3
Figure 11. Groove depth ratio	12	20	.74	.5	3 → 4

Fixed parameters: (Rotating grooves)
D_o = .0762 m
D_i = .0381 m
D_i/D_t = .5
c = 4 μm
Ω = 2000 RPM
(Λ = 5.011; Fig. 11: Λ = 5.011 → 2.227)

Fluid properties:
ρ = 1.1233 kg/m^3
μ = 1.782 × 10^{-5} Pa·s
P_i = 101.3 kPa
P_o = 517.1 kPa
Finite element parameters: No. elements rad.: 40
rad. seal dam: 10 , circ. groove, ridge: 10, 10

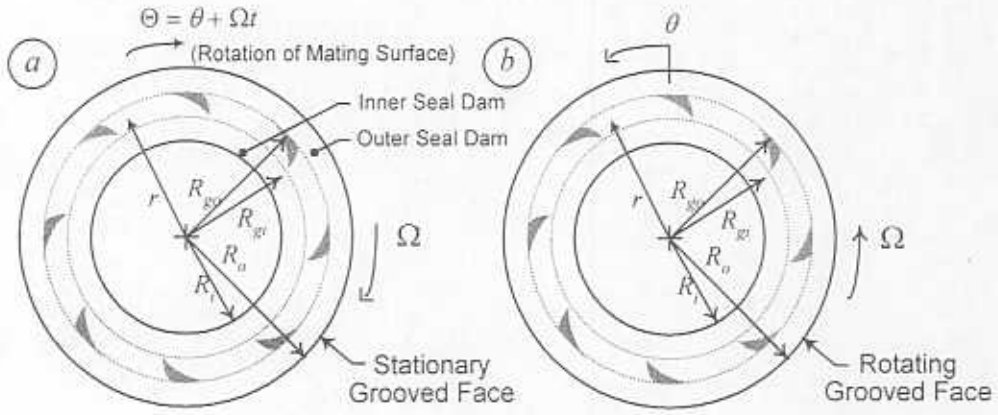

Figure 1. SGFS geometry.

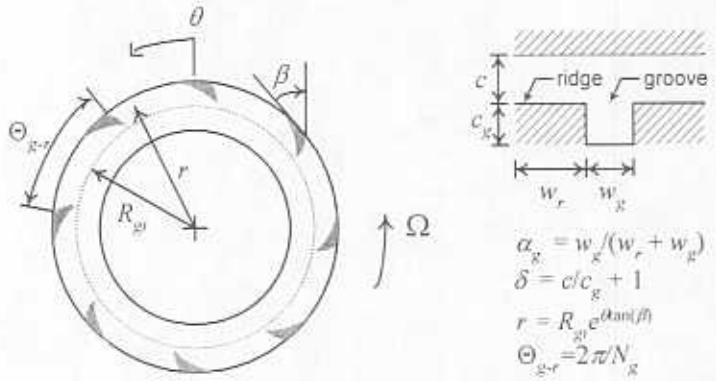

Figure 2. SGFS geometric parameters.

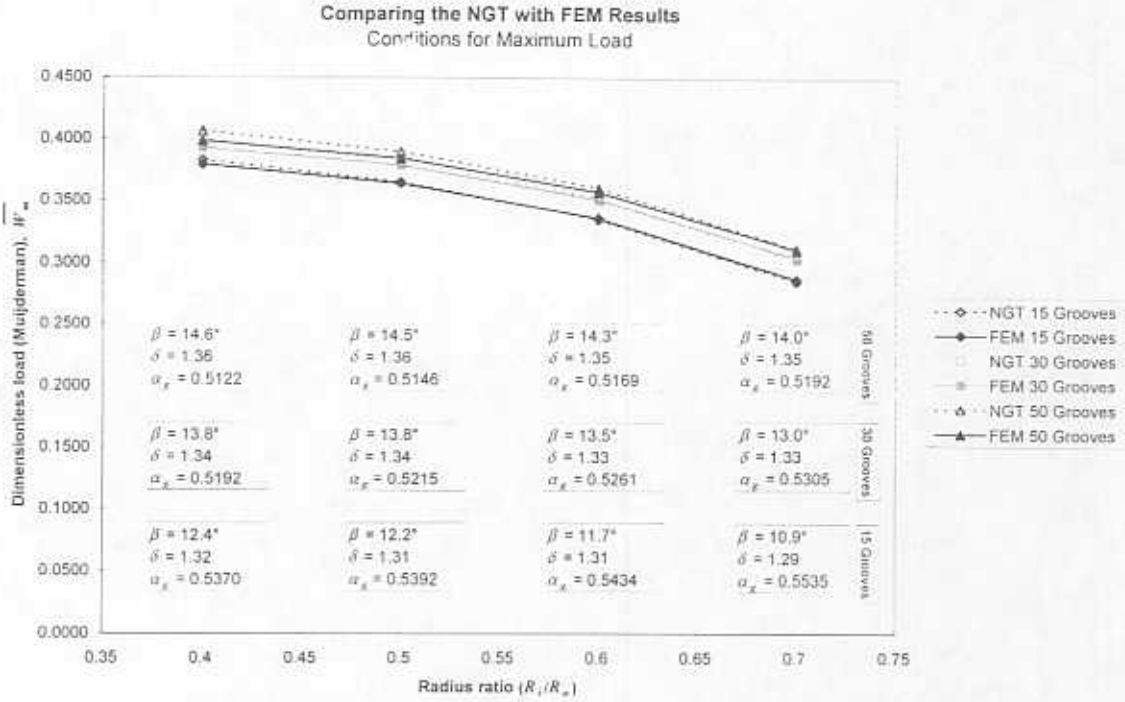

Figure 3. Comparisons of the NGT with present FEM results for dimensionless load capacity.

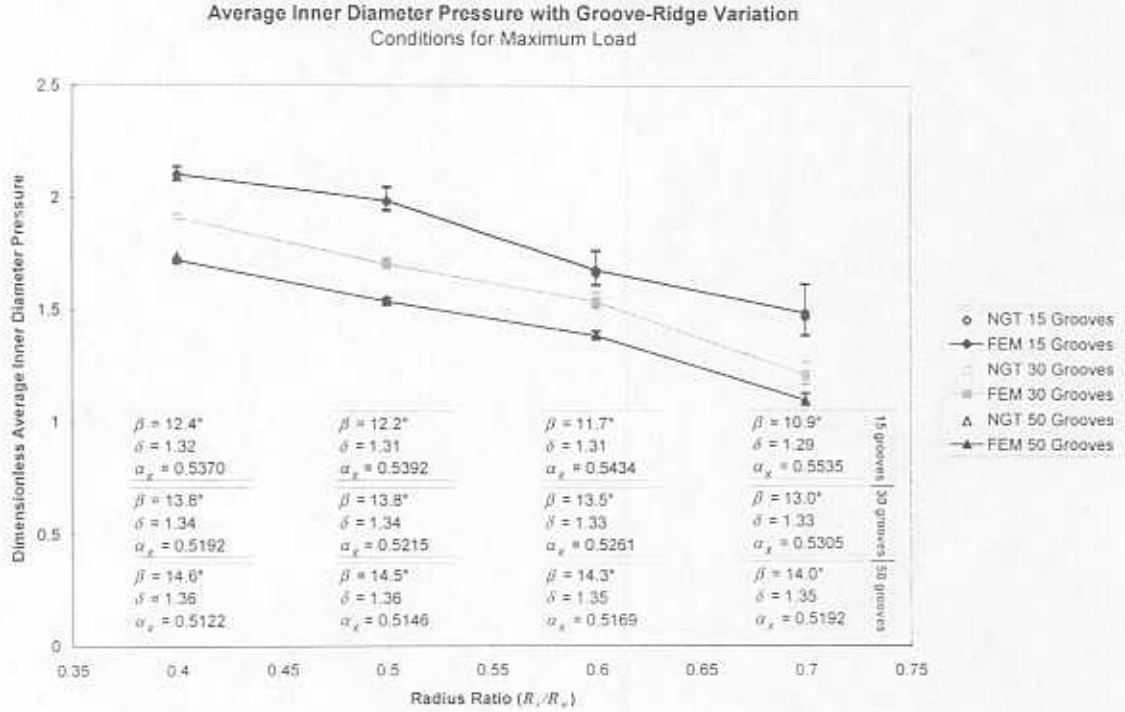

Figure 4. Calculated inner diameter pressures with variations provided by the FEM analysis.

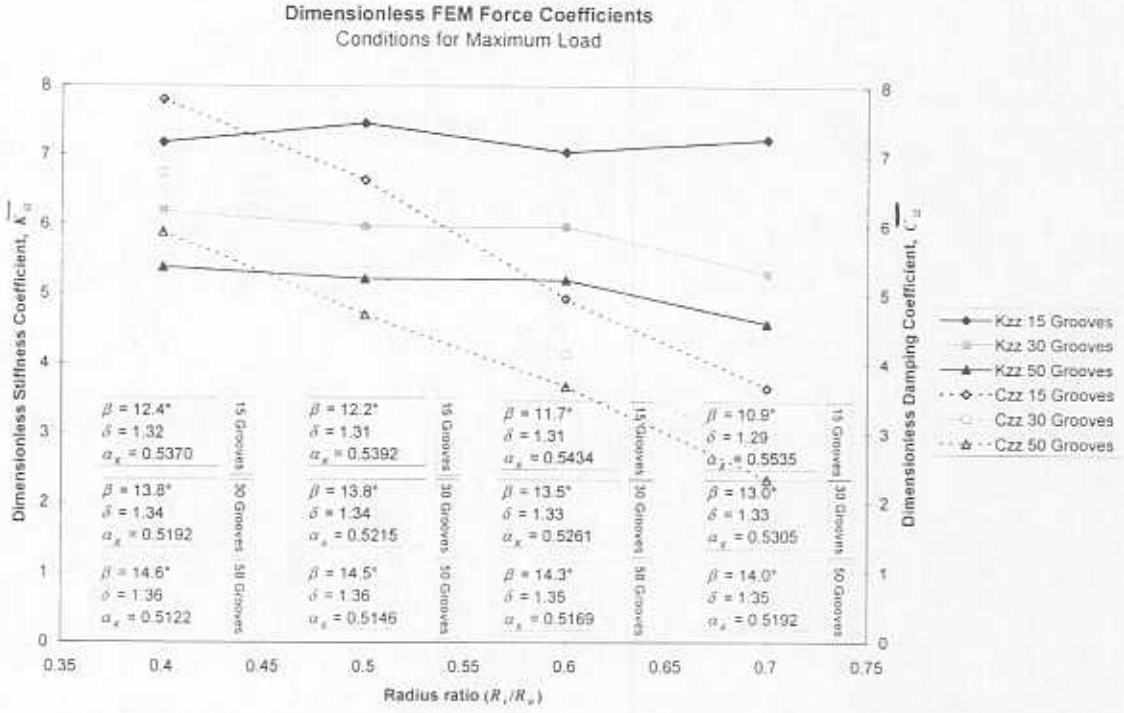

Figure 5. Dimensionless force coefficients for increasing radius ratios.

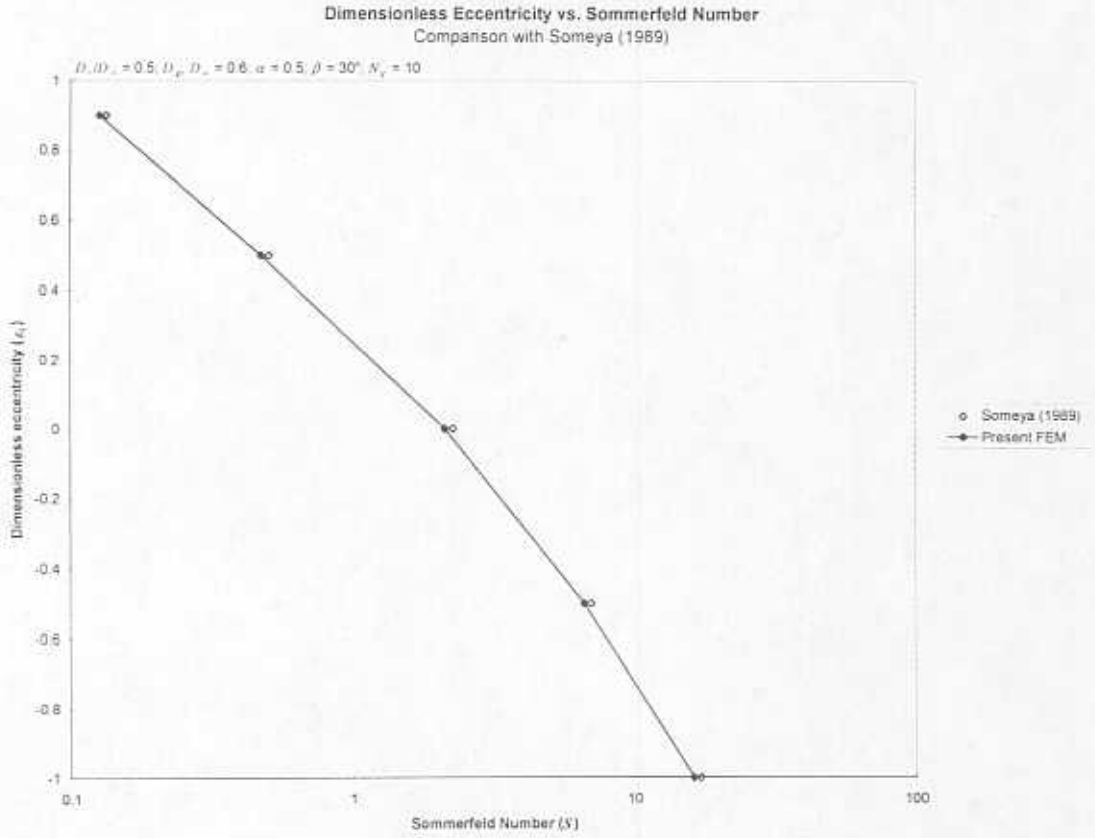

Figure 6. Comparison with Someya (1989). Sommerfeld number (S) against dimensionless eccentricity (ε_r).

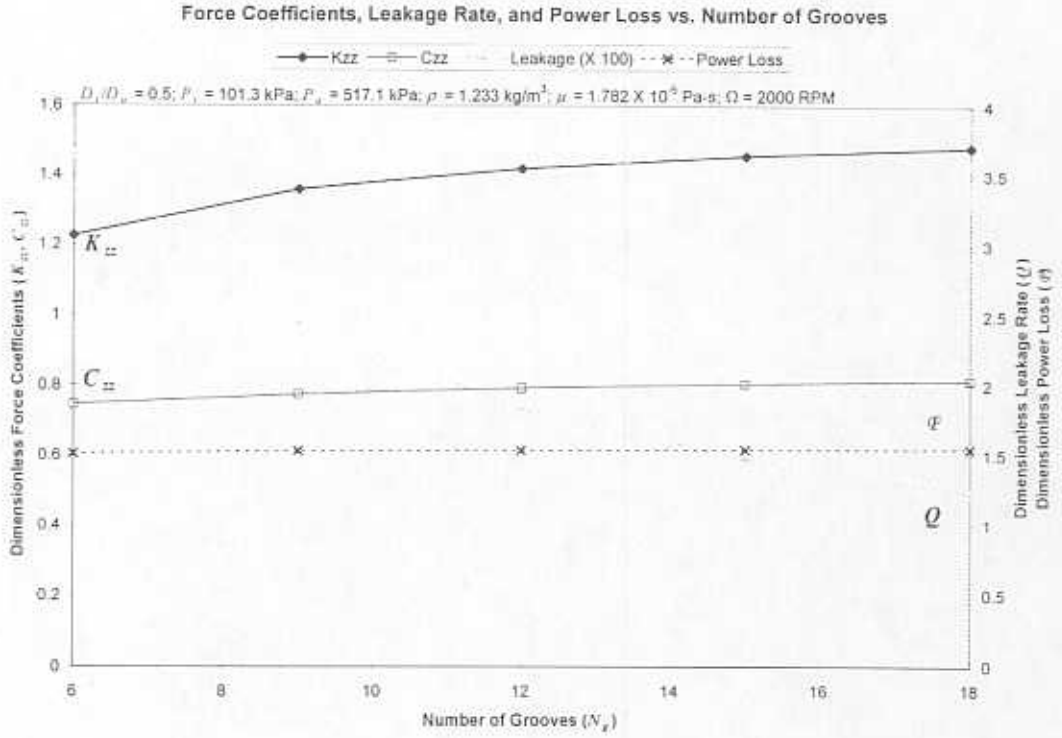

Figure 7. Variation of force coefficients, leakage rate, and power loss with the number of grooves (N_g).

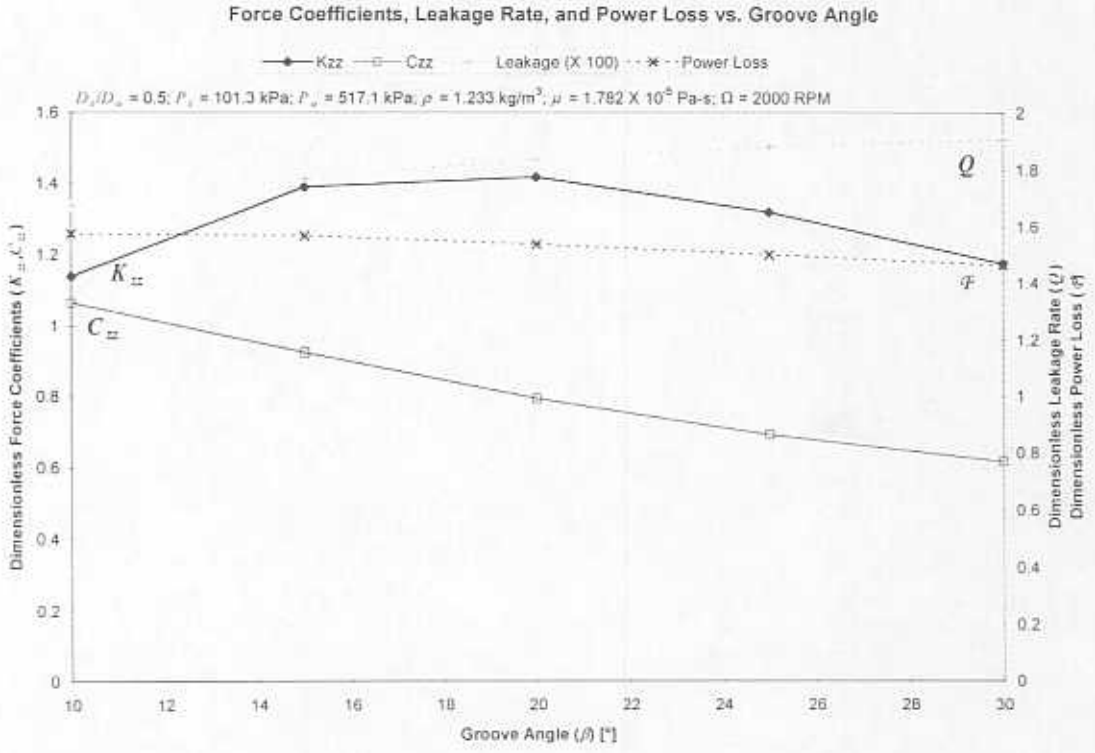

Figure 8. Variation of force coefficients, leakage rate, and power loss with groove angle (β).

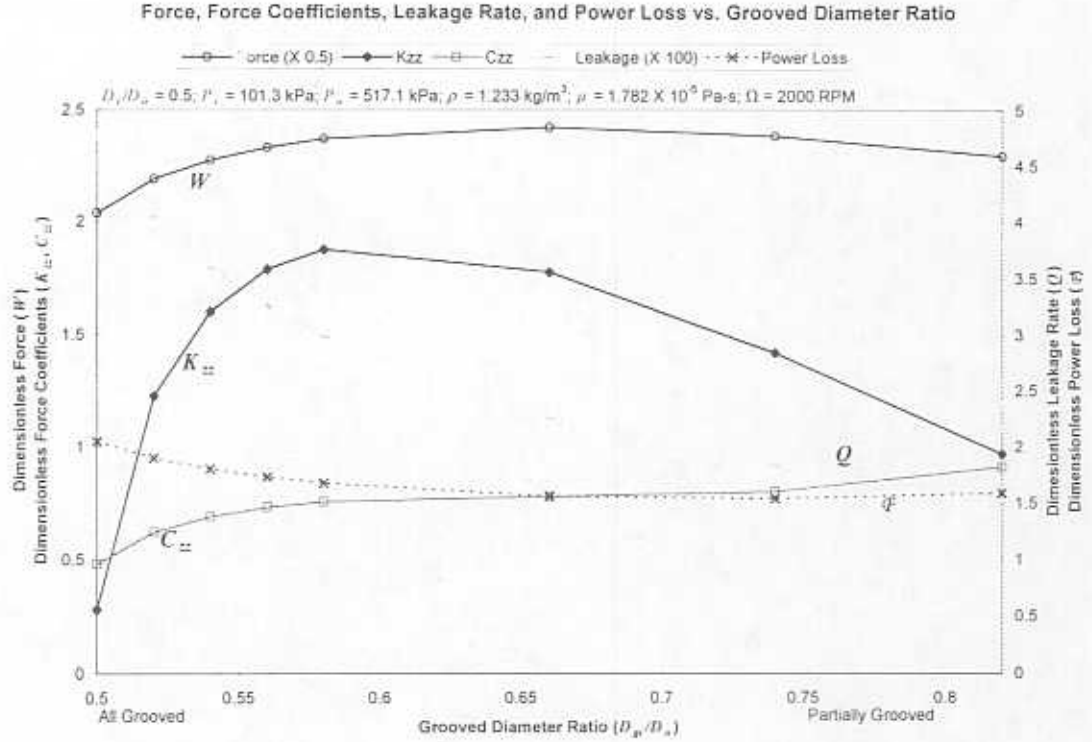

Figure 9. Variation of the opening force, force coefficients, leakage rate, and power loss with the grooved diameter ratio (D_g/D_o).

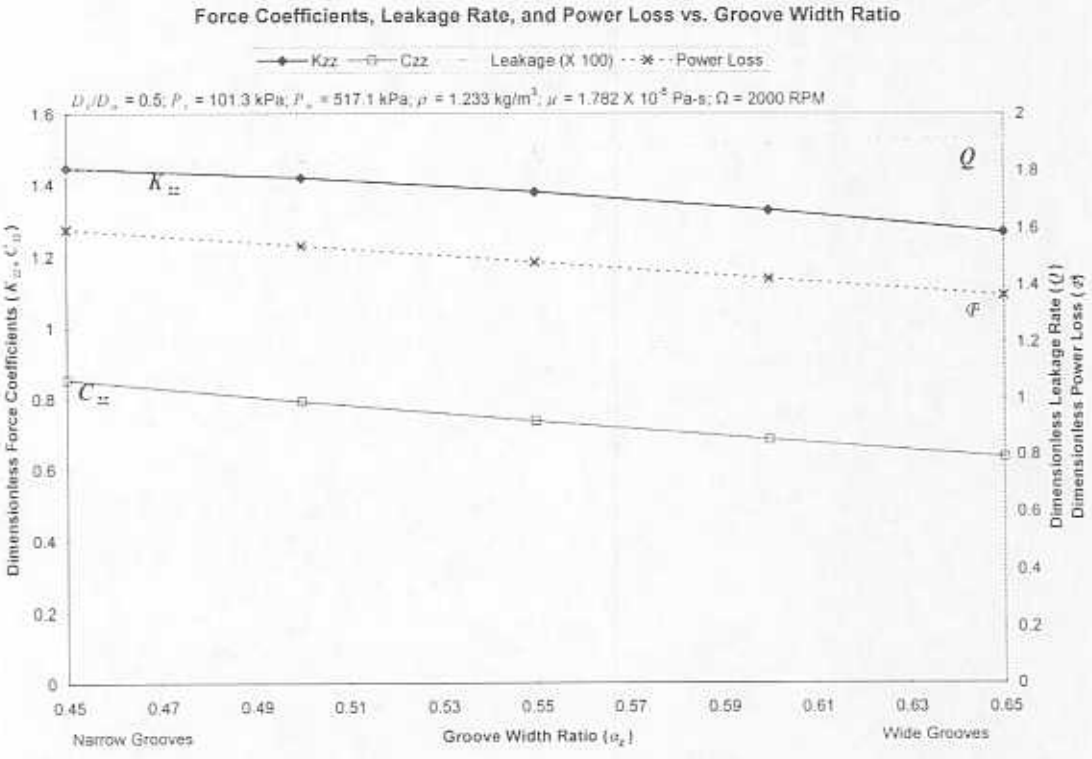

Figure 10. Variation of the force coefficients, leakage rate, and power loss with the groove width ratio (α_g).

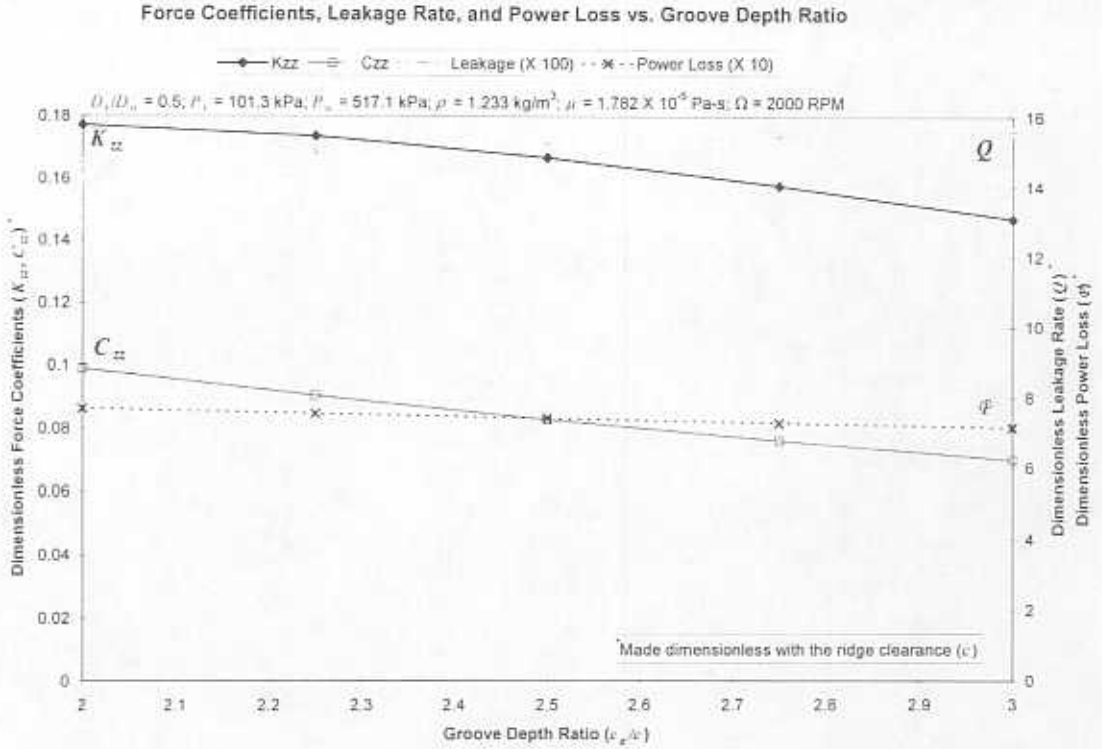

Figure 11. Variation of the force coefficients, leakage rate, and power loss with the groove depth ratio (c_g/c)

Appendix

Sample Calculation

Load and Inner Radius Pressure for SGTBs without Transverse Flow
(Muijderman, 1966)

(Names next to titles indicate which nomenc· ure is in use.)

Fixed Parameters (Zirkelback)

$R_{go} := .0425 \cdot m$

$c_g := 8 \cdot 10^{-6} \cdot m$

$N_g := 15$

$\Omega := 31.4 \cdot \frac{rad}{sec}$

$\mu := .19 \cdot 10^{-4} \cdot Pa \cdot sec$

$\rho := 998 \cdot \frac{kg}{m^3}$

Parameters for Case 1 (Zirkelback)

$R_{gi} := .0170 \cdot m$

$c := 2.56 \cdot 10^{-6} \cdot m$

$\beta := .216420827247 \cdot rad$

$\alpha_r := .537037037037$

Nomenclature (Muijderman)

h_0 : Groove depth [m]

h_1 : Film height above grooves [m] $h_1 = h_0 - h_2$

h_2 : Film height above ridges [m]

H : Groove depth ratio $H = \frac{h_2}{h_1}$

k : Number of grooves

(r,θ) : Groove coordinate system

r_1 : Inner radius of grooved part

r_2 : Outer radius of grooved part [m]

W : Load carrying capacity [N]

α : Groove angle [rad] $r = r_1 \cdot e^{\theta \tan(\alpha)}$

γ : Ratio of ridge width to groove width

η : Dynamic viscosity [N-s/m^2]

ω : Angular velocity [rad/s]

Nomenclature Conversion (M := Z)

$h_0 := c_g$

$h_1 := c - c_g$

$h_2 := c$

$H := \frac{c}{c - c_g}$

$k := N_g$

$r_1 := R_{gi}$

$r_2 := R_{go}$

$\alpha := \beta$

$\gamma := \frac{\alpha_r}{1 - \alpha_r}$

$\eta := \mu$

$\omega := \Omega$

Governing Equations (Muijderman)

Further Definitions (Equations numbers in Muijderman (1966) listed.)

Characteristic Load:

$$W_s \quad \frac{\eta \cdot \omega \cdot r_2^4}{h_2^2}$$

$$g_1 \quad \frac{\gamma \cdot H^2 \cdot \cot(\alpha) \cdot (1 - H) \cdot (1 - H^3)}{(1 - \gamma \cdot H^3) \cdot (\gamma - H^3) - H^3 \cdot \cot(\alpha)^2 \cdot (1 - \gamma)^2} \qquad (2.62)$$

$$\lambda \quad \frac{r_1}{r_2} \qquad (5.8)$$

$$C_1 \quad \frac{\exp\left(\frac{\pi}{k} \cdot \left(1 - \frac{2 \cdot \alpha}{\pi}\right) \cdot (\tan(\alpha)) \cdot \frac{2}{1 - \gamma} \cdot \frac{1 - \gamma \cdot H^3}{1 - H^3}\right) - \lambda^2 \cdot \exp\left(\frac{\pi}{k} \cdot \left(1 - \frac{2 \cdot \alpha}{\pi}\right) \cdot (\tan(\alpha)) \cdot \frac{2}{1 - \gamma} \cdot \frac{1 - \gamma \cdot H^3}{1 - H^3}\right)}{1 - \lambda^2}$$

$$p_{r1} \quad \frac{3 \cdot \eta \cdot \omega \cdot r_2^2}{h_2^2} \cdot (1 - \lambda^2) \cdot g_1 \cdot C_1 \qquad (5.7)$$

$p_{r1} = 3.54763 \cdot 10^4 \cdot \text{Pa}$ <== Pressure at the inner diameter

(5.10)

$$C_2 \quad \frac{\exp\left(\frac{2 \cdot \pi}{k} \cdot \left(1 - \frac{2 \cdot \alpha}{\pi} \cdot \tan(\alpha) \cdot \frac{2}{1 - \gamma} \cdot \frac{1 - \gamma \cdot H^3}{1 - H^3}\right)\right) - \lambda^4 \cdot \exp\left(\frac{2 \cdot \pi}{k} \cdot \left(1 - \frac{2 \cdot \alpha}{\pi} \cdot \tan(\alpha) \cdot \frac{2}{1 - \gamma} \cdot \frac{1 - \gamma \cdot H^3}{1 - H^3}\right)\right)}{1 - \lambda^4}$$

$$W_t \quad \frac{3 \cdot \pi \cdot \eta \cdot \omega \cdot r_2^4}{2 \cdot h_2^2} \cdot (1 - \lambda^4) \cdot g_1 \cdot C_2 \qquad (5.9) \qquad W \quad \frac{W_t}{W_s}$$

$W_t = 113.72334 \cdot \text{kg} \cdot \text{m} \cdot \text{sec}^{-2}$ <== NGT load capacity

$W = 0.3829$ <== NGT dimensionless load capacity